



HAL
open science

High-frequency periodic patterns driven by non-radiative fields coupled with Marangoni convection instabilities on laser-excited metal surfaces

A. Rudenko, A. Abou-Saleh, F. Pigeon, C. Maclair, F. Garrelie, Razvan Stoian, J.P. Colombier

► To cite this version:

A. Rudenko, A. Abou-Saleh, F. Pigeon, C. Maclair, F. Garrelie, et al.. High-frequency periodic patterns driven by non-radiative fields coupled with Marangoni convection instabilities on laser-excited metal surfaces. *Acta Materialia*, 2020, 194, pp.93-105. 10.1016/j.actamat.2020.04.058 . ujm-03060625

HAL Id: ujm-03060625

<https://ujm.hal.science/ujm-03060625>

Submitted on 14 Dec 2020

HAL is a multi-disciplinary open access archive for the deposit and dissemination of scientific research documents, whether they are published or not. The documents may come from teaching and research institutions in France or abroad, or from public or private research centers.

L'archive ouverte pluridisciplinaire **HAL**, est destinée au dépôt et à la diffusion de documents scientifiques de niveau recherche, publiés ou non, émanant des établissements d'enseignement et de recherche français ou étrangers, des laboratoires publics ou privés.

High-frequency periodic patterns driven by non-radiative fields coupled with Marangoni convection instabilities on laser-excited metal surfaces

A. Rudenko^{a,*}, A. Abou-Saleh^a, F. Pigeon^a, C. Mauclair^a, F. Garrelie^a, R. Stoian^a, J. P. Colombier^a

^a *Univ Lyon, UJM-Saint-Etienne, CNRS, IOGS, Laboratoire Hubert Curien UMR5516, F-42023 St-Etienne, France*

Abstract

The capability to organize matter in spontaneous periodic patterns under the action of light is critical in achieving laser structuring on sub-wavelength scales. Here, the phenomenon of light coupling to Marangoni convection flows is reported in an ultrashort laser-melted surface nanolayer destabilized by rarefaction wave resulting in the emergence of polarization-sensitive regular nanopatterns. Coupled electromagnetic and compressible Navier-Stokes simulations are performed in order to evidence that the transverse temperature gradients triggered by non-radiative optical response of surface topography are at the origin of Marangoni instability-driven self-organization of convection nanocells and high spatial frequency periodic structures on metal surfaces, with dimensions down to $\lambda/15$ (λ being the laser wavelength) given by Marangoni number and melt layer thickness. The instability-driven organization of matter occurs in competition with electromagnetic feedback driven by material removal in positions of the strongest radiative field enhancement. Upon this feedback, surface topography evolves into low spatial frequency periodic structures, conserving the periodicity provided by light interference.

1. Introduction

Self-organization into regular structures is a spectacular phenomenon, omnipresent in various competing systems in biology, geology, chemistry, soft-matter physics, hydrodynamics, nonlinear optics, and astronomy [1]. Patterns can originate from self-organization of light in nonlinear media, particularly in the presence of coherent light propagation [2–6], but also be the result of the material response, as Turing patterns in reaction-diffusion or convection systems [7–10]. From this perspective, laser-induced self-organization of matter, where the spontaneous ordering occurs as a consequence of multiscale interaction of incoming coherent light with the matter driven out-of-equilibrium, opens broad possibilities for controllable laser-induced nanostructuring. Here, the patterns are not limited to fingerprints of coherent light [11, 12], resulting in well-ordered structures with laser wavelength-related periods upon dynamic coupling of light with

light-driven evolving topography [13–15]. The patterns with dimensions far beyond the diffraction limit, relied on evanescent waves and on material response with small characteristic scales, are commonly produced [16] and are promising in view of numerous applications in optics, mechanics, and medicine [17]. All this becomes possible with the use of femtosecond laser, enabling to confine the energy at the record nanoscales without being diffused. The absorbed energy is then transferred to heat within few picoseconds, establishing high temperature gradients, resulting in localized ablation and formation of a melted nanolayer but also strong shock wave, propagating inside material, and, as a consequence, sub-surface cavitation and spallation on the timescale of few tens of picoseconds. The surface profile is then modified by melt flow until the material resolidification, after which the structures are imprinted on the surface. To achieve the regular nanopatterns with dimensions much smaller than laser wavelength, one should unavoidably rely on the global material response at the nanoscale and hydrodynamic instability to offer a realistic outlook overcoming the electromagnetic scenario constrained by non-interacting evanescent waves

*Corresponding author

Email addresses: antmipt@gmail.com (A. Rudenko), jean.philippe.colombier@univ-st-etienne.fr (J. P. Colombier)

spatially confined to surface nanofeatures. We start our discussion by analyzing the factors making possible the establishment of such instabilities. The analysis brings us towards understanding the formation mechanisms of surface periodic nanostructures with dimensions far beyond the diffraction limit. The elucidated scenarios appear to be universal allowing for generalization of laser-induced self-organization mechanisms on nano- and microscales.

1.1. Hydrodynamic instabilities

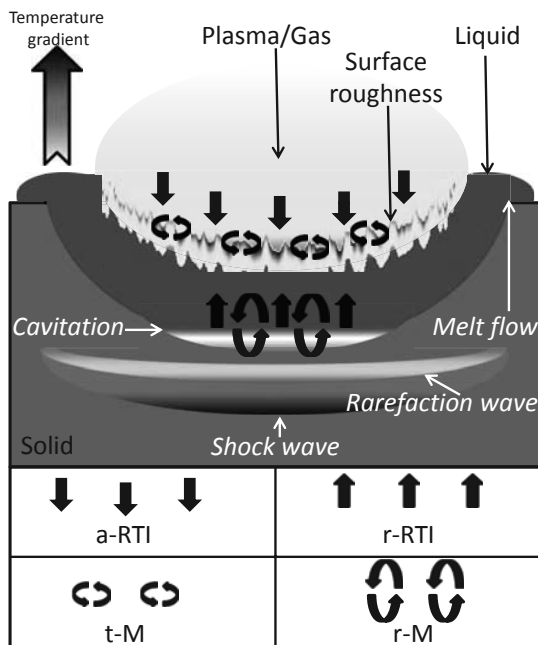


Figure 1: Ultrashort-laser induced instabilities in a liquid layer: ablative Rayleigh-Taylor instability induced by recoil pressure (a-RTI), Marangoni convection instability (hydrothermal waves) induced by transverse temperature gradients on surface nanoroughness (t-M), Rayleigh-Taylor instability induced by rarefaction wave (r-RTI), Marangoni instability driven by rarefaction (r-M). Straight arrows indicate the direction of fluid flow acceleration, curved arrows show the direction of convection velocities.

Upon ultrashort laser irradiation, strongly confined temperature gradients induce a shock wave, followed by a rarefaction wave. Such compressible behaviour of the laser-excited metals under sub-ablation irradiation conditions, results in cavitation few nanometers below the surface or spallation [18–22]. The rarefaction wave is capable to destabilize the thin liquid layer in several ways indicated in Fig. 1. Firstly, a melt layer is accelerated from

the rarefied zone towards the free surface, in the same direction that vertical temperature gradient. This effect is analog to the destabilizing effect of the gravitational force on a liquid layer heated from below, resulting in the development of Rayleigh-Bénard instability [23], or surface tension forces in Bénard-Marangoni instability [24–26]. Therefore, the system destabilized by rarefaction wave experiences Marangoni convection instability. The convection is driven by surface tension gradients, vertical (r-M) or horizontal, produced by surface inhomogeneity (t-M), taking form of cellular convection [24] or hydrothermal waves [27]. Secondly, the cavities exert a force on laser-melted layer on free surface. The described process is known as swelling, i. e. material expansion above the initial surface due to sub-surface cavitation [28]. In this case, the fluid with lower density (cavity) pushes the fluid with higher density (liquid). As a result, the conditions are satisfied for Rayleigh-Taylor instability [29–32], indicated as r-RTI in Fig. 1. Rayleigh-Taylor instability may enhance the amplitude of existing longitudinal perturbations and the contrast of surface inhomogeneity [20, 29, 32, 33]. Finally, in case of corrugated surface, rarefaction wave may result additionally in Richtmyer-Meshkov instability at contact discontinuity [34, 35]. Under strong ablation conditions and intensive evaporation, the ablative recoil force exerted on melted free surface plays also a destabilizing role and results in Rayleigh-Taylor (a-RTI) or, possibly, Richtmyer-Meshkov instabilities on the corrugated surface [20, 33, 36–38]. The occurrence of ultrashort laser-induced instabilities in liquid layers was addressed in several theoretical works supported by molecular dynamics and compressible continuous model simulations [20, 33], but commonly assuming homogeneous Gaussian energy deposition and neglecting the effects of light polarization. The Marangoni convection instability was examined at the microscale within incompressible model [39, 40].

1.2. Overview of self-organized structures

The clear signatures of a dynamic self-organization with feedback are laser-induced periodic surface structures (LIPSS) having periodicities from less than one hundred of nanometers, commonly referred to as high-spatial frequency LIPSS (HSFL), and near-wavelength periodicity (low-spatial frequency LIPSS or LSFL) up to several microns (grooves) [15–17, 21, 39–46], but also

more complex quasi-hexagonal and Turing-like patterns [36, 47–53].

The formation of LSFL with near-wavelength periodicity is commonly accepted to be the result of the interference between incident laser field and radiative scattered fields from rough surface [11, 15, 17, 21, 41–45, 54, 55]. For large band gap dielectrics, the parallel orientation and the periodicity of laser wavelength in medium is driven purely by non-plasmonic cylindrical waves, whereas both surface plasmon and cylindrical waves are involved in the formation of LSFL with orientation perpendicular to laser polarization on plasmonic metal surfaces [11, 15, 17, 45, 55, 56]. In contrast, the origin of subwavelength and suprawavelength periodic structures remains unclear [17]. It has been strongly debated for over several decades, attributing the structures either to the consequence of light interference with surface roughness and pulse-by-pulse amplification [21, 41–45, 54, 57], or hydrodynamic processes [18, 39, 40, 58, 59]. The latter may involve the instability caused by surface erosion and atomic diffusion [58], or by recoil pressure [36, 37, 49], cavitation-induced instability [18, 19, 60] and, more recently, Marangoni convection instability and thermocapillary waves [39, 40, 46, 59]. The diversity of the proposed scenarios is due to the specificity of periodic structures, inheriting both the properties of light (e. g. laser polarization) and the hydrodynamic properties such as bifurcation and coalescence in fluid dynamics. The latter are similar to the properties of the structures created by ion-beam sputtering [48, 61]. The electromagnetic approaches considering light interaction with surface inhomogeneities predict polarization-dependent distribution of non-radiative scattered fields on rough surfaces with strong dispersion of high spatial frequencies [41, 43, 62]. This results in quasi-periodic patterns via pulse-by-pulse feedback mechanisms, such as ablation processes, surface tension or recoil pressure-driven melt flows [37, 41, 54, 63]. Here, the roughness is not limited to pristine irregular topography but can be induced by laser, for example, as in the regimes of spallation and sub-surface cavitation [18, 20–22], Rayleigh-Taylor instability in thin melt layer [20], or material redeposition on the surface [64]. Noteworthy, the formation of regular HSFL on the surface and so-called self-organized nanogratings in the bulk of transparent materials [65] with periodicity approaching half-laser wavelength in medium [57, 66] perpendicular to laser

polarization was explained by periodic nanoplasma arrangement driven by coherent superposition of scattered waves at surface or bulk inhomogeneities [5, 6, 45]. However, these deep-subwavelength nanostructures should be distinguished from their counterparts on metal surfaces [17], where the optical absorption is dominated by free carrier absorption, HSFL are oriented parallel or perpendicular to laser polarization [22, 43], and the periodicity is independent of laser wavelength [19]. The last-mentioned fact, as well as the irregularity and the dispersion of subwavelength absorption patterns even from homogeneous concentration of surface roughness centers after few feedback cycles in contrast to regular ripples observed experimentally by one or two pulse irradiation [43] make the scenarios restricted to an electromagnetic mechanism to explain the HSFL formation mechanism at least questionable. Worthy to mention, the electromagnetic-based models with intra-pulse feedback [41, 43, 54] always neglected thermal diffusion, which is capable to make the temperature distribution uniform and even more dispersed, erasing the fingerprints of light at the nanoscale. Regarding the hydrodynamic simulations, the empirical models based on Kuramoto-Sivashinsky equations were applied to investigate the variety of possible Turing patterns resembling the structures induced by laser irradiation or ion-beam sputtering [49, 58]. However, these approaches do not allow to relate the laser-irradiation conditions to the resulting patterns and to elucidate the exact physical mechanisms contributing to the development of surface instability. The formation of microstructures such as grooves and spikes was then explained by Tsibidis et al. based on the solution of incompressible Navier-Stokes equations, indicating the generation of hydrothermal waves and convection rolls for low and high Prandtl number fluids accordingly due to thermal gradients created by previously formed LSFL [39, 40]. Nevertheless, the existing models fail to explain the formation of regular HSFL with orientations both perpendicular and parallel to laser polarization and periods down to $\lambda/15$ on metal surfaces [22, 43], as well as more complex morphologies, consisting of hierarchical periodic surface structures [19, 21, 22, 43, 59, 60, 67–69] and quasi-hexagonal arrangements [36, 47, 49–53, 70, 71]. For instance, the transitions between HSFL and LSFL are contradictory discussed in the literature, where both lithographic scenarios, based on electromagnetic field enhancement between regular rectangu-

lar grooves and period reduction or grating splitting [57, 72–75], and hydrodynamic scenarios based on the instability [48, 59, 60] were proposed. Field enhancement on subwavelength sinusoidal grating, for instance, does not result in period reduction [15]. Additionally, a variety of HSFL periods different from half of LSFL periods were reported, with HSFL at the border of laser-affected zone, where less energy is deposited [22, 43, 76, 77]. Regarding the hexagonal nano- and microstructure self-organization, several plausible scenarios were proposed revealing similarities with Bénard-Marangoni or other convective instabilities [47, 53, 69, 71], but also dewetting in thin liquid films [50], and Rayleigh-Taylor instabilities [30, 36, 49]. To our best knowledge, none of these scenarios have been verified by numerical modeling.

In this article, we develop a model combining three-dimensional electromagnetic and hydrodynamic approaches. This allows us to investigate the multipulse evolution of surface relief in a self-consistent way, recalculating the energy distribution on the corrugated surface at the beginning of each pulse and taking into account both liquid melt flow and ablation processes. In contrast to previously proposed incompressible hydrodynamic model [39, 40, 63], we solve compressible Navier-Stokes equations supplemented by the equation of state and consider the deformable free surface. This allows us to take into account pressure wave propagation induced by temperature gradients, as well as ablative recoil pressure acting on a liquid layer. Additionally, inhomogeneous absorption on surface roughness calculated by Maxwell equations provides a whole variety of initial perturbations and anisotropic temperature gradients for generation of hydrothermal waves and forced liquid melt flows [27, 78].

We show that the convection instability develops in thin laser-melted layers destabilized by rarefaction wave. Activated by transverse temperature gradients resulted from surface roughness, the melt flow follows Marangoni surface tension forces up to surface resolidification. Such an instability drives the matter towards self-organized convection nanocells, and, being sensitive to polarization dependence, to connected periodic stripes with sub-wavelength spacings, resembling HSFL structures, commonly observed upon multipulse laser irradiation. The numerical results explain also the transition from HSFL to LSFL structures for higher laser irradiation dose [19, 22, 67–69, 76, 77, 79–82], where

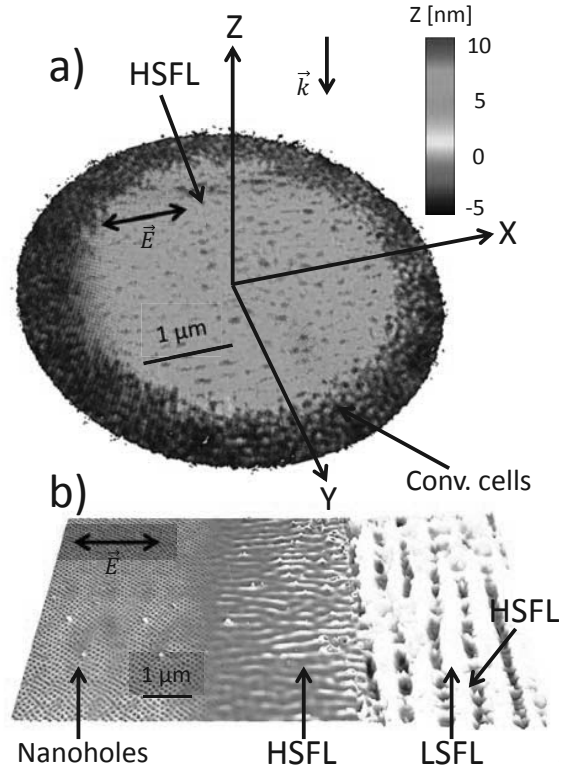


Figure 2: (a) Schematics of the considered problem. Numerical simulations show the surface topography upon single pulse irradiation of nickel, where the structures of interest are indicated: HSFL (high-spatial frequency LIPSS) and convection cells in form of nanoholes. The colors correspond to the surface depth Z . (b) Scanning electron microscopy images of surface topography upon irradiation of nickel by 20 double pulses with the peak fluence $F = 0.24 \text{ J/cm}^2$ indicate three different types of nanostructures while increasing the energy from the left to the center of laser spot: hexagonal nanoholes, HSFL, and LSFL (low-spatial frequency LIPSS). Pulse duration is 150 fs, laser wavelength is 800 nm [71].

the LSFL structures are shown to have a fully electromagnetic origin and to be formed by material removal.

2. Numerical model

Multiphysical three-dimensional simulations are performed, based on Maxwell equations taking into account inhomogeneous energy deposition on rough surface [62], a two-temperature model to resolve electron-ion heat transfer and diffusion [83], and compressible Navier-Stokes equations [84], written

in the form of the conservation laws for energy, momentum and mass [26, 63, 83, 85, 86] as follows

$$\begin{cases} \rho C_i \left[\frac{\partial T_i}{\partial t} + \vec{u} \cdot \nabla T_i \right] = \nabla \cdot (k_i \nabla T_i) \\ \frac{\partial(\rho \vec{u})}{\partial t} + (\vec{u} \cdot \nabla)(\rho \vec{u}) + (\rho \vec{u}) \nabla \cdot \vec{u} = \\ = -\nabla(P_e + P_i) + \mu \nabla^2 \vec{u} + \frac{1}{3} \mu \nabla(\nabla \cdot \vec{u}) \\ \frac{\partial \rho}{\partial t} + \nabla \cdot (\rho \vec{u}) = 0, \end{cases} \quad (1)$$

where \vec{u} is the fluid velocity, ρ and T_i are the ion density and temperature, P_e is the electronic pressure evaluated based on the results of ab initio calculations [87], P_i is the lattice pressure evaluated by equation of state (EOS) [88], μ , C_i and k_i are the viscosity, the heat capacity and the thermal conduction, whose temperature dependencies are taken from Ref. [89, 90]. The thermo-capillary boundary conditions are introduced at liquid free surface [26, 85, 86] as follows

$$\begin{cases} \frac{\partial u_x}{\partial z} = -\gamma/\mu \frac{\partial T_i}{\partial x} \\ \frac{\partial u_y}{\partial z} = -\gamma/\mu \frac{\partial T_i}{\partial y}, \end{cases} \quad (2)$$

where (u_x, u_y, u_z) are the components of \vec{u} , and γ is the surface tension coefficient [91]. The deformable free surface is treated via volume-of-fluid (VOF) method [92]. A detailed description of the numerical model is given in Supplementary Material. We perform simulations for stainless steel and nickel, their optical and thermophysical parameters are also discussed in Supplementary Material.

We consider the surface dynamics upon laser irradiation by Gaussian femtosecond pulses up-down Z axis and laser polarization along X axis indicated in Fig. 2. Here and further, the laser wavelength is 800 nm and the pulse duration is fixed to be 80 fs in numerical calculations. We are interested in surface topography modifications at the nanoscale, which are the result of liquid melt flow and material removal. In our simulations, the density snapshots are taken 100 ps after irradiation. Within this time, we consider that the ablated material is removed and the fluid movement is finalized. Further calculations do not influence the material redistribution and show the trends of rapid cooling and resolidification. For instance, Fig. 2(a) indicates the formation of periodic surface structures with periods ≈ 150 nm parallel to the laser polarization in the center of the laser-irradiated zone by material redistribution above the initial surface. This

result is consistent with experimental observations of HSFL on nickel surface in Fig. 2(b) and previous experiments [16, 71]. On the borders of the laser-heated region, the convection cells in the form of nanoholes are formed. Similar structures were observed by multipulse femtosecond laser irradiation of nickel in Fig. 2(b). The lowest energy dose here corresponds to hexagonal nanoholes of ≈ 80 nm spacings and ≈ 20 nm in diameter. Closer to the center of the laser-irradiated zone, HSFL oriented parallel to laser polarization with periods ≈ 150 nm are observed. Finally, LSFL with periods ≈ 600 nm oriented perpendicular to laser polarization occupy the center of the laser-irradiated zone. Additionally, the sequence of parallel HSFL can be seen between neighbor LSFL crests forming a mixed structure of crossed LIPSS. The formation of periodically packed nanoholes, nanoprotusions, and nanoparticles were reported in several papers on the surface of tungsten [93, 94], silicon [36, 53] and, more recently, germanium [70], or nickel [71]. In case of nanometric holes with sub-100 nm spacing on the nickel surface, specific surface and ultrashort laser treatment was required in order to avoid the symmetry breaking by the influence of laser polarization and consequent formation of LIPSS. More precisely, a mono-crystalline Ni sample is used and the self-organization is driven by multiple sequence of cross-polarized double pulses. The experimental results are discussed in Ref. [71]. In our simulations, we observe the self-organization of nanoholes for similar energy dose but much wider laser irradiation conditions. However, this is attributed to the fact that the density morphology representing closely packed nanoholes obtained in a wide range of simulations does not necessary result in permanent modifications.

3. Marangoni instability

Under femtosecond laser irradiation, the absorbed energy on the surface is inhomogeneously confined on the nanoscale due to the presence of pristine or laser-induced nanoholes or nanobumps at the origin of high local electric field enhancement [21, 62]. As a result, strong temperature gradients of order $\Delta T = 200$ K/nm are established in the transverse plane below the surface. Inhomogeneously heated melt flow is driven by surface tension-driven Marangoni forces, redistributing the material from hot spots to colder zones on free surface. These forces are predominant at relatively

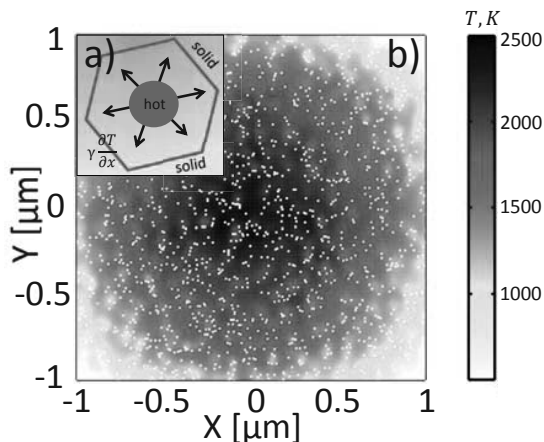


Figure 3: Marangoni convection on anisotropically heated surface. (a) The melt front upon fluid flow driven by Marangoni forces caused by an isolated hot spot. (b) Surface-tension driven temperature redistribution upon irradiation of nickel surface with random hot spots colored in white. The temperature snapshot is taken 50 ps after laser irradiation.

low irradiation conditions, when the recoil pressure forces arising during evaporation of liquid film can be neglected. At the same time, the energy is dissipated by thermal diffusion, finally resulting in a complete stop of the melt front and resolidification upon lattice cooling. However, under extreme conditions of the energy confinement in a thin liquid layer and sufficiently high temperature gradients, convective heating can overcome the cooling effects, rendering the system unstable.

The primary instability that can develop in a thin melted layer is a convection instability analogical to Bénard-Marangoni instability [24–26], albeit driven by transverse temperature gradients [27, 39, 95]. In case of laser interaction with surfaces, the vertical laser-induced temperature gradients are directed towards free surface. This is in contrast to classical scenario of heating from below [24], where the temperatures increase from free surface towards volume and the gravitational force plays a destabilizing role. As a result, a force directed towards the temperature gradient is required to destabilize the system irradiated by laser. For instance, destabilization occurs as a result of laser-induced rarefaction wave towards free surface, as shown in Fig. 1. The developed Marangoni instability results in self-organization into convection cells with dimensions few times exceeding the melt layer depth

$\Lambda = 2\pi L/\sqrt{Ma/8}$ [26, 85, 86, 96], where L is the melt layer depth, $Ma = \frac{\gamma\Delta T_i L}{\mu D_i}$ is the Marangoni number, and $D_i = k_i/\rho C_i$ is the thermal diffusivity. In classical case of Bénard-Marangoni instability, this longitudinal Marangoni number should be higher than the critical value in the range of $Ma_{cr} = 40 - 80$ to develop the instability [24–26]. In contrast, in case of deformable free surface, it was proven that such a condition was not required, as the cellular convection instability occurred even for indefinitely small Marangoni number [95]. For example, typical values for nickel at the melting point $T_m = 1727$ K are $k_i \approx 40$ W/m/K, $\rho \approx 7900$ kg/m³, $\gamma = 0.4 \cdot 10^{-3}$ N/m/K, $\mu \approx 3 \cdot 10^{-3}$ Pa·s, and $C_i \approx 630$ J/kg/K. One can estimate the thermal diffusivity $D_i \approx 8 \cdot 10^{-6}$ m²/s, Marangoni number $Ma \approx 0.4 - 2$, depending on the melt layer depth $L = 10 - 50$ nm, and typical pattern size $\Lambda \approx 60 - 180$ nm. The characteristic timescales for Marangoni flow $\tau_{t-M} = \frac{\mu\Lambda^2}{4L\gamma\Delta T} \approx 100 - 500$ ps [37], which is less than the typical melt layer lifetime for the ablation threshold energy dose [97]. However, as the melt layer is destabilized by rarefaction wave, gaining negative pressures of order $P \approx 5$ GPa [21], the timescales of rarefaction wave-accelerated flow $\tau_{r-M} = \frac{\mu\Lambda^2}{PL^2} \approx 25$ ps are much shorter. This characteristic time can be derived analogically to the one for Marangoni flow by replacing the surface tension gradient by force induced by pressure differences in the rarefied substance and melt layer of thickness L . Fig. 3(a) shows a convection cell created by the interplay of Marangoni forces and thermal diffusion applied to a single hot spot, which can be induced by local field enhancement below a nanohole. The instability would redistribute the matter over the free surface into the most compact hexagonal way, whereas the dimensions of the cell are related to Marangoni number and, consequently, the ratio between the destabilizing Marangoni force and the viscous restrictive force. Furthermore, the self-organization of convection patterns is obtained for a random distribution of hot spots shown in Fig. 3(b), indicating that the cell dimensions are almost independent of the initial positions of white-colored hot spots or initial surface roughness. They also slightly vary depending on the position from the center of laser spot and, consequently, local laser fluence. The latter dependence comes from the characteristic dimension $\Lambda \propto \sqrt{L}$, increasing with the increasing liquid layer depth. This proportionality is due to

the fact that $Ma \propto L$ and $\Lambda \propto L/\sqrt{Ma}$.

Noteworthy, the absorption inherits the polarization memory of the light, therefore, the temperature gradients and the initial perturbations are asymmetric in the transverse plane. The upper row in Fig. 4 indicates the absorbed energy distribution below the surface with a single nanobump or a nanohole in propagation (with the wave-vector \vec{k} indicated) and transverse planes. The red color indicates the most affected zones, which would possibly melt or be ablated by ultrashort pulse. The particularity of such energy deposition is the strong polarization dependence with orientations parallel to laser polarization in case of nanobumps and perpendicular to laser polarization in case of nanoholes [62]. Anisotropic temperature gradients result in the development of convection rolls and hydrothermal waves in a thin liquid layer [27, 78]. The nature and the orientation of the resulting standing waves is defined by Prandtl number $Pr = C_i\mu/k_i \approx 0.05$, which equals the ratio between viscosity and thermal diffusivity. For liquid metals, heat diffuses very quickly, resulting in $Pr \ll 1$ and leading to hydrothermal waves perpendicular to transverse temperature gradients [27, 39].

Fig. 4(a, b) illustrates the preferential direction of standing hydrothermal wave launched by single nanobump and nanohole. Counterintuitively, holes induce convection patterns parallel to laser polarization, whereas bumps contribute to the development of patterns oriented perpendicular to laser polarization. In order to verify this scenario, we calculate the material redistribution upon femtosecond laser irradiation of nickel surface with initial random distribution of nanobumps and nanoholes. We keep the equivalent sub-ablation irradiation conditions. The density snapshots demonstrating the melt flow patterns (white-colored) above solid surface (black-colored) after 100 ps of irradiation are shown in Fig. 4(c, d). In both cases, we observe quasi-periodic patterns with periodicity ≈ 300 nm, resembling HSFL. The pattern orientation is perpendicular to laser polarization in case of initial bumpy surface, but parallel in case of random nanoholes. The presence of laser-induced sub-surface nanobubbles or opened nanovoids, being precursors of parallel-oriented HSFL, was evidenced on the surface of aluminium, nickel, and titanium in several works [18, 19, 21, 68]. We conclude that the preferential orientation of the patterns depends on the nature of the initial surface roughness.

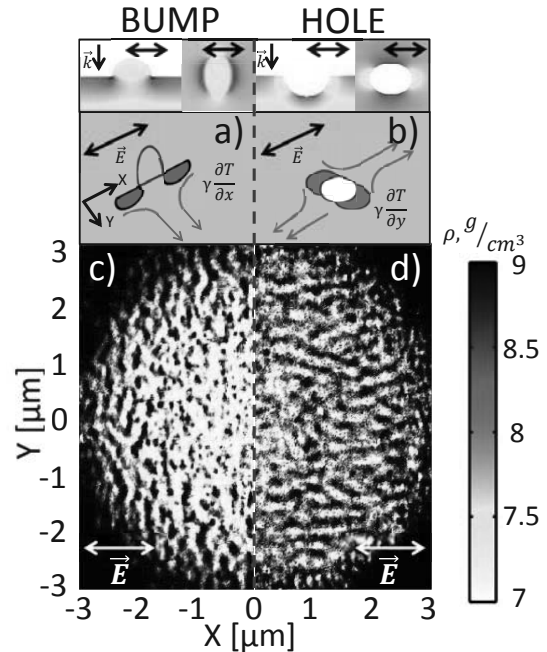


Figure 4: Mechanisms of convective instability development upon irradiation of surfaces with random (a) nanobumps and (b) nanoholes is illustrated. Upper images indicate the absorbed energy in the vicinity of a single nanofeature in propagation and transverse planes. Then, the direction of fluid flow from hot spots near bumps/holes is shown by red lines. The resulting density snapshots upon irradiation of surface with (c) nanobumps and (d) nanoholes of $R = 5$ nm with concentration $C = 2\%$ indicate the formation of HSFL oriented (c) perpendicular or (d) parallel to laser polarization. Laser fluence is $F = 0.25$ J/cm². The lattice density distributions are shown 100 ps after laser irradiation.

However, local orientation slightly varies, which indicates on the hydrodynamic nature of the patterns and the orientation defined by non-uniform melt layer. In contrast to high-spatial frequency electromagnetic field patterns, the density patterns are less dispersed, more connected, and more pronounced at the borders of the laser-affected zone.

The polarization-dependence of the electromagnetic response is the reason why the instabilities on transverse temperature gradients, taking the form of convection roll-like patterns, dominate over classical cellular convection instability in thin laser-melted layers. Therefore, we will focus mainly on the phenomenon of light polarization and Marangoni flows coupling. The closely packed nanoholes are, however, observed in simulations for low energy dose. This energy is sufficient to acti-

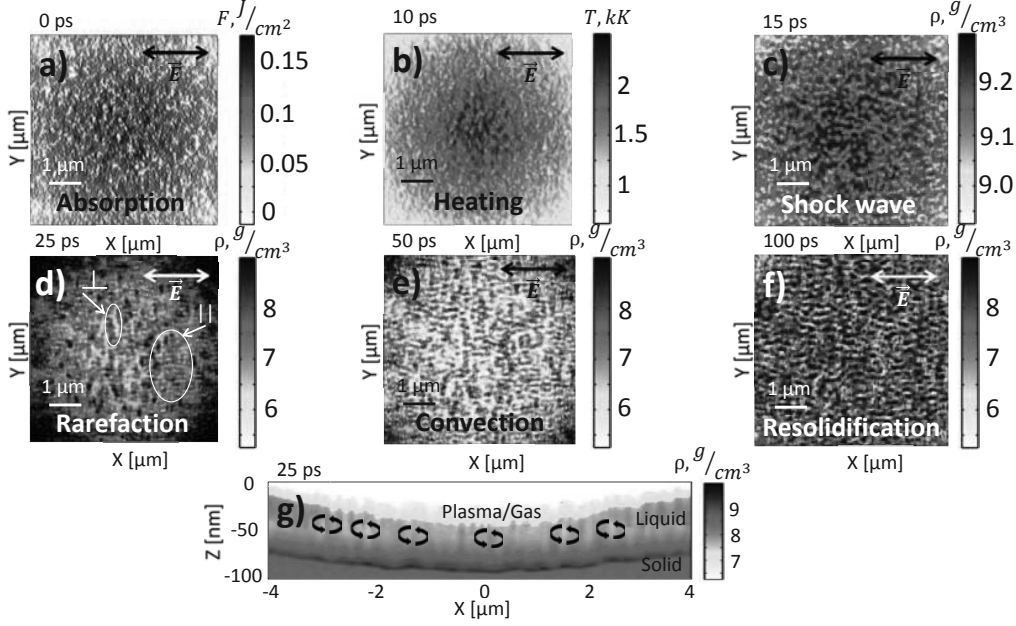


Figure 5: Surface dynamics upon ultrashort laser irradiation with peak fluence $F = 0.5 \text{ J/cm}^2$. (a) Absorbed energy on the initial surface, (b) maximum temperature distribution, and density snapshots (c-f) in the transverse and (g) in the propagation plane are shown. The time is indicated (a-f) on the top of the corresponding figures. The initial surface roughness consists of random nanoholes of $R = 5 \text{ nm}$ with $C = 2\%$ concentration. The arrows in (g) represent fluid velocities upon convection.

vate hot spots below random nanocavities, induced by previous laser pulses, but not enough to melt the surrounded polarization-dependent regions.

The dynamics of self-organization is further illustrated in Fig. 5. The process is initiated by inhomogeneous energy absorption below random nanoholes in Fig. 5(a), where the electromagnetic patterns are strongly dispersed but have the preferential orientation perpendicular to laser polarization, referred to type-r (roughness-dependent) in the literature [41, 43, 45]. The corresponding maximum lattice temperature distribution is further shown in Fig. 5(b), repeating the general features of the electromagnetic pattern after electron thermal equilibrium at $t = 10 \text{ ps}$. If only the thermal diffusion is taken into account, the patterns are further spread over the Gaussian laser spot, where the high-spatial frequency memory is lost within $\approx 100 \text{ ps}$. However, the lattice density is strongly influenced during this time by inhomogeneous shock wave and rarefaction below the surface. These processes are essential to destabilize the system, as self-organization occurs only if the compressible effects are considered. The corre-

sponding density snapshots at $t = 15 \text{ ps}$ and $t = 25 \text{ ps}$ are shown in Fig. 5(c, d). The primary material response is chaotic, where only the memory of discrete hole positions, with the largest amount of absorbed energy, is transferred within the shock wave. Then, the region starts to melt reaching densities below $\rho = 7.9 \text{ g/cm}^3$. Fig. 5(d) discloses the melt regions still conserving the perpendicular orientation to laser polarization given by light (marked as \perp) and the initiation of surface tension-driven flows perpendicular to these hot zones, i. e. parallel to laser polarization (marked as \parallel). The corresponding density variations in the propagation plane are revealed in Fig. 5(g), indicating the presence of counter-rotating rolls confined between solid state, with a shock wave propagating downwards, and liquid melted region. We note that the convection occurs in the transverse plane, whereas the term "roll" indicates that the roll-like patterns are formed by rolling fluid movement of hotter fluid over the colder one driven by surface tension forces within a single cycle. The patterns produced by stationary hydrothermal waves are pronounced already at $t = 50 \text{ ps}$ timescale in Fig. 5(e). Further

surface evolution is characterized by lattice cooling, whereas Marangoni forces become weaker, and pattern establishment and resolidification, starting from $t = 100$ ps timescale in Fig. 5(f). At this time, if the temperature gradients are high enough, the hot matter is redistributed over the cold lattice above the initial surface, resulting in HSFL with subwavelength periods and parallel orientation as shown in Fig. 2(a). The time for complete resolidification depends on laser fluence and is found to be in the range of 250 – 500 ps in our simulations.

The importance of both destabilizing laser-induced rarefaction wave and surface tension-driven gradients in subwavelength pattern formation can be understood by a simple analysis of the equations (1) and thermo-capillary boundary conditions (2). In fact, the temperature gradients in the transverse plane $[\frac{\partial T_i}{\partial x}, \frac{\partial T_i}{\partial y}]$, created by inhomogeneous energy absorption and heating, result in longitudinal gradients of transverse fluid velocities $[\frac{\partial u_x}{\partial z}, \frac{\partial u_y}{\partial z}]$, pushing the hot melt fluid above the cold one. The longitudinal rarefaction wave amplifies the longitudinal fluid velocities u_z due to the elevated pressure gradients $\frac{\partial P}{\partial z}$ via momentum conservation along z axis. The destabilizing force is directed along temperature gradients, pushing the liquid above the initial surface. Therefore, both Marangoni forces and rarefaction wave act constructively via the term $[u_z \frac{\partial u_x}{\partial z}, u_z \frac{\partial u_y}{\partial z}]$ in momentum conservation along x and y directions, influencing the density distribution $\rho(x, y)$ via mass conservation. Note that the fluid movement would not occur in case of homogeneous heating, resulting in negligible transverse fluid velocity gradients, or in case of incompressible scenario with no rarefaction, where u_z would play stabilizing role.

The pattern growth could be further amplified by Rayleigh-Taylor instability [29, 30, 38], which occurs when a thin laser-melted layer is destabilized by rarefaction wave or by recoil pressure under ablative irradiation conditions, as shown in Fig. 1. According to the dispersion relation, the patterns are amplified if they have wavelength larger than $\Lambda = 2\pi\sqrt{\frac{2\sigma}{\rho a}}$ [29, 38], where a is the acceleration of lighter fluid (vapour, rarefied fluid) towards denser fluid (liquid), and σ is the surface tension. For $a \approx 10^{13}$ m/s², driven by pressure gradients of order $\nabla_z P \approx 100$ MPa/nm, $\Lambda \approx 50$ nm, whereas the time required for the instability development is on picosecond timescale $\tau_{RTI} = \frac{12\eta\sigma}{L^3\rho^2 a^2} \approx 13$ ps for liquid layer depths of $L = 10$ nm [36, 37]. The disper-

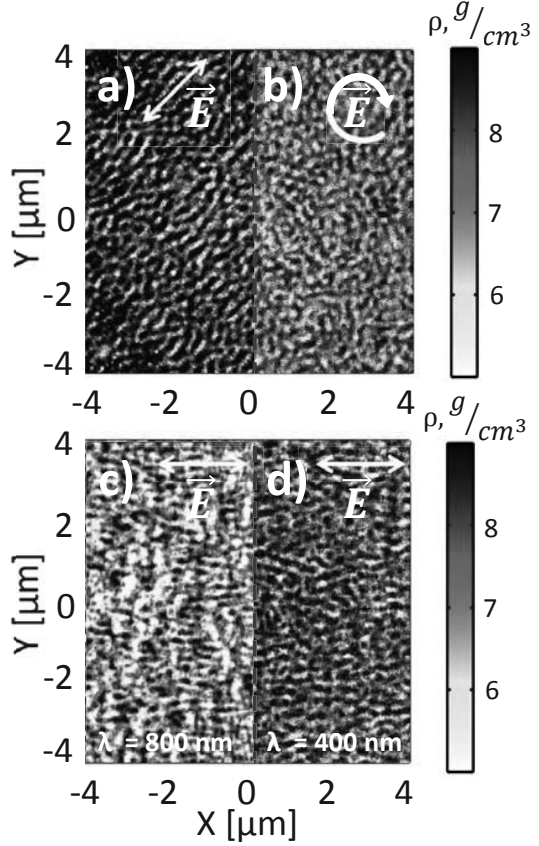


Figure 6: Influence of laser polarization (a, b) and laser wavelength (c, d) on the resulting patterns. Liquid density distributions on nickel surface irradiated by peak fluence $F = 0.25$ J/cm² laser pulses with (a) linear $\pi/4$ and (b) circular polarizations; linear polarization and wavelengths (c) $\lambda = 800$ nm, (d) $\lambda = 400$ nm. The initial surface roughness consists of random nanoholes of $R = 5$ nm with $C = 2\%$ concentration. The lattice density distributions are shown 100 ps after laser irradiation.

sion relation, however, indicates that smaller critical wavelengths are selected upon stronger laser irradiation conditions, which contradicts the observation of HSFL for sub-ablation irradiation conditions and microstructures, such as spikes and grooves, for significantly higher laser energy dose. The direct influence of Rayleigh-Taylor instability on the nanostructures is not evidenced from numerical simulations. As follows from the impact of material properties, such as viscosity and surface tension, or laser parameters, such as laser fluence, on the nanostructure characteristics, the dimensions do not follow the dispersion relation for Rayleigh-Taylor instabil-

ity, but correlate well with the characteristic wavelengths for Marangoni instability.

4. Pattern properties

4.1. Laser polarization affecting the orientation

The influence of the electric field polarization on the lattice density profiles are investigated by keeping the identical initial surface roughness, consisting of nanoholes. The patterns follow the laser polarization, turning ninety degrees if we switch the polarization along axis X to the polarization along axis Y . This property of HSFL on metal surfaces has been previously reported [19]. For instance, Fig. 6(a) shows the patterns created by ultrashort laser pulse with $\pi/4$ -inclined polarization. We note that the structures are entirely the consequence of melt flow on the surface with initially randomly distributed nanoholes giving irregular and dispersed absorption below the surface. This way, the material redistribution occurs in more complex way, than just in electromagnetic scenario supported by intra-pulse feedback [41, 54]. The periodicity remains unchanged while modifying the polarization state of light. We also show that labyrinth-like Turing patterns [98, 99] are obtained by applying circular laser polarization in Fig. 6(b). Here, the local orientation of the nanostructures is defined by complex profile of melted layer below rough surface. The pattern is more uniform, with high number of pronounced nanoholes.

4.2. Laser wavelength

Another interesting result is that the nanostructure periodicity is not sensitive to laser wavelength. The calculations are performed with $\lambda = 800$ nm and $\lambda = 400$ nm and the resulting nickel density snapshots are shown in Fig. 6(c, d), indicating the same dimensions of the structures, which proves the fact that the ordering is not given by the interference of light but has hydrodynamic origins. Similar conclusions were made based on the experimental results for HSFL on titanium surface [19]. Interestingly, this dependence is different from HSFL and nanogratings induced on the surface and in the bulk of dielectrics [66], where the self-ordering takes place during laser pulse irradiation on sub-picosecond timescale and is driven by the interference and consequent electron density evolution [5, 6, 45].

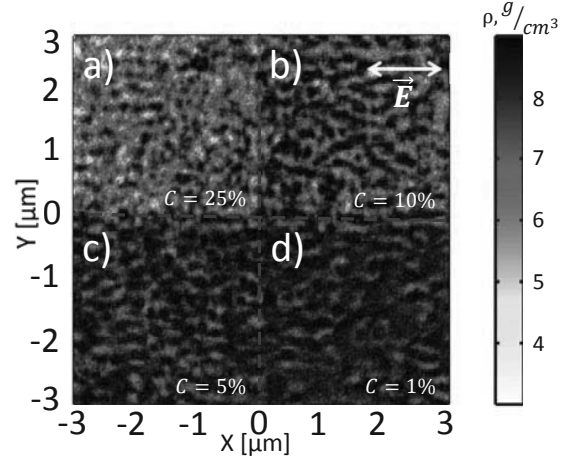


Figure 7: Influence of initial surface inhomogeneity on the resulting patterns. Liquid density distribution on nickel surface irradiated by peak fluence $F = 0.25$ J/cm² laser pulse with different initial nanohole concentrations (a) $C = 25\%$, (b) $C = 10\%$, (c) $C = 5\%$, and (d) $C = 1\%$ of $R = 5$ nm. The pattern periodicity does not correlate with inhomogeneity concentration. The lattice density distributions are shown 100 ps after laser irradiation.

4.3. Concentration of rough centers

The influence of the initial nanohole concentration on nanostructure periodicity and regularity is then investigated. As expected, small or very high concentration of nanoholes does not lead to any self-organization, but only to local random laser-induced melting. Surprisingly, when the nanostructures are created, even strong differences in nanohole density and different initial distributions do not influence the pattern periodicity. Fig. 7 shows the resulting pattern upon irradiation of a single laser pulse on differently arranged surface but equivalent irradiation conditions. Although the morphology varies considerably in all the cases, from completely melted region in case of high concentration in Fig. 7(a) down to almost solid state in Fig. 7(d), similar structures are formed. This result underlines the principle differences between the absorbed energy patterns, as a consequence of light interaction with non-radiative fields, and material density patterns established upon fluid flow driven by Marangoni convection instability. For electromagnetic patterns, the increase of inhomogeneity concentration causes shifting to higher frequencies [43, 62]. This effect is amplified by positive feedback provided by free carrier density kinetics on the surfaces and in the bulk of dielectrics, resulting

into regular electron density patterns with periodicity proportional to a fraction of laser wavelength in medium [5, 45]. However, the simulations with coupled electromagnetics and hydrodynamics for metals support an alternative scenario, where the hydrothermal waves establish the pattern dimensions independent of the frequency given by non-radiative electromagnetic response.

4.4. Material properties affecting the periodicity

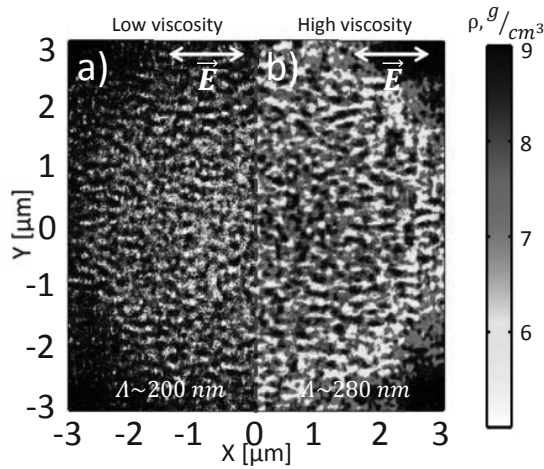


Figure 8: Influence of material viscosity on the resulting patterns. Liquid density distribution on nickel surface irradiated by $F = 0.25 \text{ J/cm}^2$ fluence laser pulse with different viscosity (a) $\mu = 2 \cdot 10^{-3} \text{ Pa}\cdot\text{s}$ and (b) $\mu = 4 \cdot 10^{-3} \text{ Pa}\cdot\text{s}$ and initial nanohole concentration $C = 2\%$. The average periods of the nanostructures are indicated. The lattice density distributions are shown 100 ps after laser irradiation.

The periodicity of HSFL can be slightly controlled by changing laser fluence. In fact, the thickness of melt layer increases with the fluence as $\Lambda \propto \sqrt{L}$. The period increase with the increasing laser fluence was evidenced in few experimental works on titanium surface [19, 68, 100]. Apart from the melt layer thickness, the material characteristics, such as viscosity and thermal diffusivity, dependent on laser-induced temperatures, influence the final result, as $\Lambda \approx 4\pi\sqrt{\frac{2\mu D_i L}{\gamma \Delta T}}$, therefore, different periods can be obtained on different metals. The given expression is obtained while putting the Marangoni number expression into the formula for characteristic size of the convection cells $\Lambda = 2\pi L / \sqrt{Ma/8}$ [26, 85, 86, 96]. Numerical simulations confirm that the pattern dimensions increase

approximately $\propto \sqrt{\mu}$ while increasing twice artificially the viscosity of nickel from $\mu = 2 \cdot 10^{-3} \text{ Pa}\cdot\text{s}$ to $\mu = 4 \cdot 10^{-3} \text{ Pa}\cdot\text{s}$. The results are shown in Fig. 8, where the patterns obtained within larger viscosity are thicker and less dense than the analogous structures formed within lower viscosity and the periodicity increases from $\Lambda \approx 200 \text{ nm}$ to $\Lambda \approx 280 \text{ nm}$. The lowest feasible periodicity of the nanostructures is related to the lowest uniform liquid layer or the absorption depth of metals in the range of 10 – 20 nm. For instance, the melt layer thickness of $L = 10 \text{ nm}$ would result in patterns with dimensions as small as $\Lambda \approx \lambda/15$. The electron diffusion can be another limiting factor for specific laser irradiation conditions/surface topography/material [17, 101, 102]. In fact, if the electron-phonon coupling time is long enough and the electron diffusion is strong enough, the hot spots with the highest electron temperatures might be diffused or even homogenized if they are close enough to each other [17, 102]. The electron-phonon coupling factor is strongly material-dependent, and nickel is a metal with extremely low factor ($\gamma = 10^{17}$) $\text{Wm}^{-3} \text{ K}^{-1}$ for $T_e = 2 \cdot 10^4 \text{ K}$ and, thus, pronounced electron diffusion during electron-ion heat transfer exchange. Comparing the absorbed energy distribution in Fig. 5(a) and ion temperature distribution in Fig. 5(b), one confirms that the effect of diffusion as a result of weak electron-ion coupling is significant, and the frequency spectrum is broader than of the initial intensity pattern (not periodic/discrete-random but almost homogeneous). Our finding is that, even in this case, the temperature gradients would be strong enough to redistribute melt flows into periodic patterns $\Lambda \approx 150 - 300 \text{ nm}$ as a result of Marangoni convection, independent of the actual initial concentration of these hot spots and "roughness-produced high spatial frequencies". The influence of electron diffusion is much smaller for the materials with high electron-phonon coupling factor, such as stainless steel ($\gamma = 3 \cdot 10^{18}$) $\text{Wm}^{-3} \text{ K}^{-1}$ for $T_e = 2 \cdot 10^4 \text{ K}$ or titanium ($\gamma = 2.75 \cdot 10^{18}$) $\text{Wm}^{-3} \text{ K}^{-1}$ for $T_e = 2 \cdot 10^4 \text{ K}$, therefore, smaller periodicity is expected down to the values limited by melt layer depth $\Lambda \approx 50 - 75 \text{ nm}$. From the other point of view, the stronger the local field enhancement is, the stronger contrast and inhomogeneity in temperature profile remains, therefore, the necessary temperature gradients can still be obtained in case of more significant roughness or laser irradiation by higher number of pulses required to develop such roughness. One notable example is

the HSFL structures formed between the crests of the LSFL structures. In fact, strong light confinement in the hollows of LSFL cannot be withdrawn by strong electron diffusion and the Marangoni instability takes place. Another example is the local field enhancement on laser-induced cavities below the irradiated surface. Again, further irradiation results in opening of voids, indicating that the light confinement dominates over electron thermal diffusion effects. The nanoscale temperature gradients then should be enough to destabilize the melt flow redistributing it into the smallest periodic patterns.

4.5. Thermal properties affecting the orientation

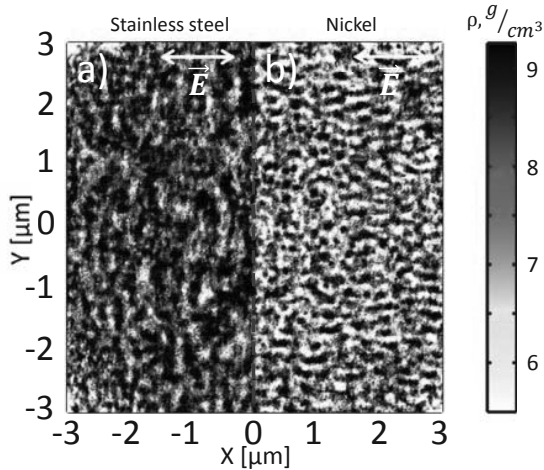


Figure 9: Influence of the material properties on the resulting patterns. Liquid density distribution on (a) stainless steel irradiated by peak fluence $F = 0.15 \text{ J/cm}^2$ and (b) nickel surface irradiated by peak fluence $F = 0.25 \text{ J/cm}^2$ with equally mixed concentration of nanoholes and nanobumps with concentrations $C = 2\%$ and $R = 5 \text{ nm}$. Fluences are chosen to create similar sub-ablation conditions upon laser irradiation for both materials. The lattice density distributions are shown 100 ps after laser irradiation.

Apart from slight dependence on material properties, we find that the dominant orientation of patterns is also affected by the thermal properties of metal. In fact, the local field enhancements induced by holes are typically more pronounced and decay slower below the surface than the ones induced by bumps of equivalent size. The absorbed energy is further transformed into heat, where temperature gradients strongly confined below the surface may inherit the polarization memory of any

inhomogeneities, whereas weaker temperature gradients are affected only by thermal response of the holes. The heat penetration depth varies according to metals, influenced mostly by electron-phonon coupling constant γ_{ei} [101]. For instance, ultra-short laser-induced nickel has one of the lowest values of γ_{ei} with $\gamma_{ei}^{Ni} = 1.1 \cdot 10^{17} \text{ W/m}^3/\text{K}$ at the electron temperature $T_e = 20000 \text{ K}$. In contrast, the electron-phonon coupling is extremely strong for stainless steel with $\gamma_{ei}^{SS} = 31.7 \cdot 10^{17} \text{ W/m}^3/\text{K}$ at the same temperature [103]. Strong energy confinement in case of stainless steel is favourable for gaining the polarization non-radiative response of short distance-acting bumps, whereas more important melt layer thickness in case of nickel is favourable for the polarization response of long distance-acting holes. In order to compare the response of these two different metals, we start with the initial conditions, providing equivalent random distribution of nanoholes below the surface and nanobumps above the surface, having mixed optical response. Surprisingly, the perpendicular-oriented patterns appear in case of stainless steel, however, parallel-oriented HSFL are pronounced on nickel surface in Fig. 9. Generally, the parallel-oriented structures are formed more easily than their perpendicular-oriented counterparts. We expect that the material preference for particular type of structures is related to the ability to confine the energy and, particularly, γ_{ei}/k_i values. For instance, HSFL- \parallel are commonly created on nickel [21, 67], aluminium [18, 67], and titanium [19, 60, 68, 80] surfaces, whereas HSFL- \perp are typically observed on the surface of stainless steel [76, 77], tungsten [43], and copper [79]. Noteworthy, the surface roughness is modified pulse-by-pulse, therefore, rather complex scenarios are involved if periodic structures are already formed with a certain orientation, partly discussed in the next section of the article.

5. Multipulse simulations

Surface topography evolves upon irradiation by multiple femtosecond laser pulses. Redistribution of the absorbed energy on the modified surface driven by positive electromagnetic feedback may cause the appearance of different types of periodic structures, resulting in hierarchical ripple patterns. After having discussed the properties of subwavelength patterns formed by a single pulse, we investigate possible feedback mechanisms and variety of structures, obtained by multipulse irradiation. Fig.

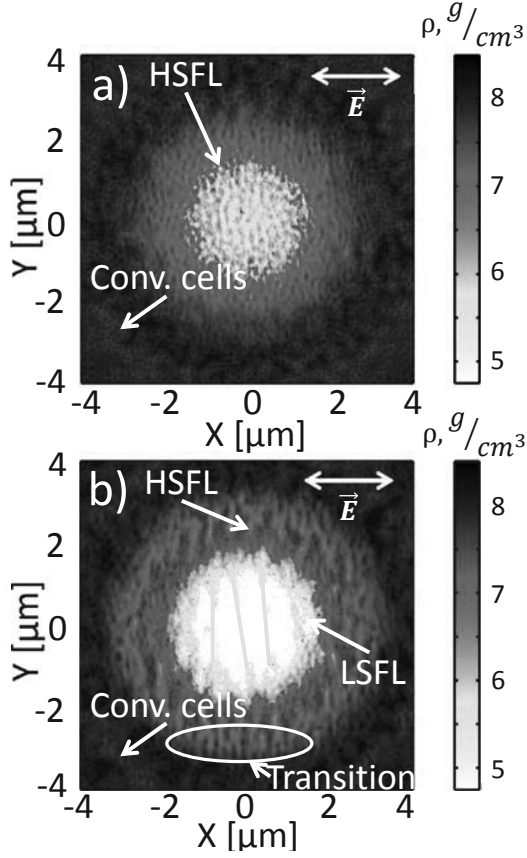


Figure 10: Topography transition from HSFL- \perp to LSFL structures in multipulse irradiation of stainless steel. Liquid density distribution on stainless steel surface irradiated by peak fluence $F = 0.15 \text{ J/cm}^2$ after (a) $N = 2$ and (b) $N = 5$ pulses. The initial surface roughness consists of random nanobumps of $R = 5 \text{ nm}$ with $C = 2\%$ concentration. The lattice density distributions are shown 100 ps after laser irradiation.

10(a) shows the lattice density snapshot 100 ps after $N = 2$ pulse irradiation of bumpy stainless steel surface. As expected, temperature gradients parallel to laser polarization created by non-radiative response of nanobumps lead to the excitation of perpendicular-oriented hydrothermal waves. As a result, the subwavelength structures with $\approx 150 \text{ nm}$ periodicity and orientation perpendicular to laser polarization are formed in the center of the laser-affected zone. At the borders of this region, cellular convection instability takes place resulting in closely packed nanohole arrangements. Self-organization here is due to lower energy dose, which is not enough to melt the polarization-dependent

regions but is sufficient to activate Marangoni flows from inhomogeneously distributed hot spots. The fact that only HSFL (and not LSFL) are formed by $N = 2$ pulse irradiation is because HSFL are triggered by the material hydrodynamic response, already pronounced at the early stage of laser-surface interaction if the initial roughness is present and occurs even if the peak fluence is below the single-pulse ablation threshold. In contrast, the onset of LSFL requires the ablative material removal in the hollows. This effect is amplified pulse by pulse [84] (the quasi-periodic distribution of the absorbed energy, however, is from the very first pulse [12, 21, 43]) and becomes dominant over the melt flow only after $N = 5$ pulses in Fig. 10(b). Thus, irradiation by a higher number of pulses results in more complex patterns, established by the interplay between electromagnetic and hydrodynamic processes. For instance, LSFL with orientation perpendicular to laser polarization and periodicity $\approx 650 \text{ nm}$ are created in the center of the laser-affected region by ablation feedback (white-colored), whereas HSFL are still present at the border of the crater with slightly larger periodicity $\approx 200 \text{ nm}$. Such a complex pattern with mixed type of structures was observed in several experiments [43, 72–74]. Our results indicate that HSFL structures are formed here not by LSFL splitting, as previously proposed [72–74], but by Marangoni instability independent of the periodic material removal by ablation in the center of laser spot resulting in LSFL. Finally, closely-packed nanoholes are also present, with slightly larger spacings. Both for periodic nanostructures and convection cells, the increase of their dimensions is attributed to deeper melt layer thickness, as a result of enhanced absorption produced by created structures. Similar topography transitions are also obtained in case of the initial surfaces with randomly distributed nanoholes. For instance, Fig. 11 shows the transition from HSFL- \parallel to LSFL on nickel surface irradiated by multiple sub-ablation threshold pulses. Interestingly, the energy of the first pulse is not enough to ablate the surface and only HSFL structures are created as the result of surface tension-driven convection instability in Fig. 11(a). The second pulse removes the material from discrete zones further transformed into connected LSFL by ablation. Both structures are seen after $N = 3$ and $N = 5$ pulses irradiation in Fig. 11(c, d). LSFL occupy the center of laser-affected region, whereas parallel oriented HSFL are between LSFL and sur-

round these structures. Similar patterns with co-existent LSFL and HSFL- \parallel are commonly observed in experiments [21, 22, 43, 59, 69]. Our simulations indicate that both types of structures are created independently by different mechanisms.

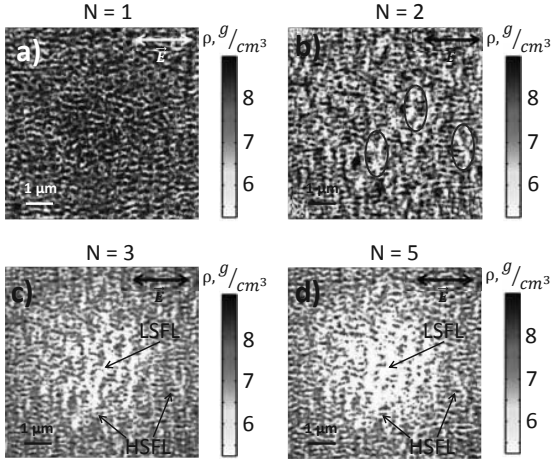


Figure 11: Topography transition from HSFL- \parallel to LSFL structures in multipulse irradiation of nickel. Liquid density distribution on nickel surface irradiated by peak fluence $F = 0.25 \text{ J/cm}^2$ after (a) $N = 1$, (b) $N = 2$, (c) $N = 3$, and (d) $N = 5$ pulses. For $N = 2$, the regions, where LSFL start to appear, are underlined by blue ellipsoids. The initial surface roughness consists of random nanoholes of $R = 5 \text{ nm}$ with $C = 2\%$ concentration. The lattice density distributions are shown 100 ps after laser irradiation.

We perform also three-dimensional multipulse simulations to elucidate the evolution of LSFL under ablation conditions corresponding to laser fluence $F = 0.5 \text{ J/cm}^2$. In order to decrease the number of required pulses, we take the initial distribution of low density $C = 0.5\%$ but large size $R = 50 \text{ nm}$ nanoholes. Such a distribution was shown to be favourable for the development of LSFL due to more pronounced role of radiative absorption [21]. The energy absorption on the initial surface and on the modified surface after $N = 5$ pulses is plotted in Fig. 12(a). The positions of holes or void-like structures are white-colored to indicate the surface topography. At the initial surface, electromagnetic radiative patterns oriented perpendicular to laser polarization and having near-wavelength periodicity are pronounced. The highest energy is absorbed near the holes, as a consequence of the interference with non-radiative scattered fields. The consecutive irradiation by several pulses results in the ablation

of hot spots on the surface, corresponding both to radiative and non-radiative responses. As a result, the matter acquires the polarization-dependent topography with amplified LSFL structures. Some additional features can be revealed if we analyze the density distribution 100 ps after pulse irradiation in Fig. 12(b). Between the LSFL crests, smaller structures are formed parallel to laser polarization with periods $\approx 200 \text{ nm}$, resembling cross-oriented HSFL commonly observed in experiments [21, 22, 43, 59, 68, 69]. We note that the energy is absorbed in the hollows of the LSFL structures mostly perpendicular to laser polarization, amplifying the pre-existent gratings. There is no periodic subwavelength field enhancement parallel to laser polarization. The HSFL structures are here the consequence of the melt flow above the LSFL hollows and the HSFL ridges are upraised by surface tension-driven melt flow. The instability is developed after LSFL structures were created. Strong temperature gradients perpendicular to laser polarization below ripple holes trigger the development of hydrothermal waves in the direction parallel to laser polarization and, as a consequence, HSFL- \parallel formation. Apart from near-wavelength and sub-wavelength nanostructures, we note quasi-periodic parallel oscillations in both absorbed energy and density maps, resembling grooves with periodicity $\approx 2.5 \mu\text{m}$. In this particular case, however, they are the consequence of inhomogeneous energy absorption on the surface, as previously reported in several theoretical works [41–44].

Table 1 summarizes the types of periodic structures commonly observed on metal surfaces, their precursors, origins of their periodicity and orientation, and feasible feedback mechanisms for their formation based on this work and several previous theoretical works. We notice that the surface inhomogeneity is the precursor for all the organized structures. As a result of light interference with scattered fields from surface topography, the energy is anisotropically distributed on laser-excited surfaces. The absorbed energy distribution is a consequence of non-radiative (short-distance and confined to nanoscale features) and radiative (long-distance and laser wavelength-related) optical responses of rough surface [43, 62]. Two major multipulse feedback scenarios are then possible to drive the matter into self-organized nanostructures. The electromagnetic scenario relies on the selection of the unique wavelength-related frequency for surface topography, where the light follows the topography

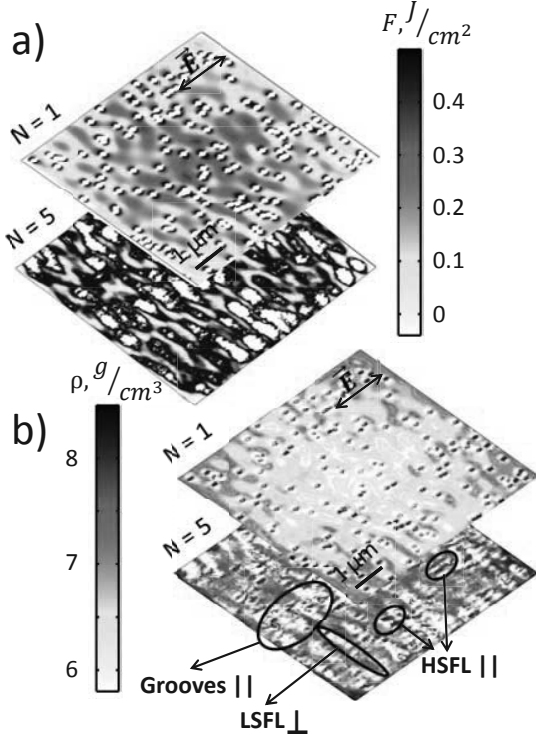


Figure 12: Variety of patterns formed by multipulse irradiation of stainless steel. (a) Absorbed energy and (b) density distribution after $N = 1$ and $N = 5$ pulses irradiation in the transverse section of corrugated stainless steel surface. Peak laser fluence is $F = 0.5 \text{ J/cm}^2$. The lattice density distributions are shown 100 ps after laser irradiation.

and the topography is modified by light pulse-by-pulse via material removal at the regions of the highest absorbed energy [15, 41]. This is possible due to coherent nature of the radiative optical response, but also due to positive feedback, resulting in the amplification of patterns with particular periodicity. In contrast, the (radiative or non-radiative) optical response can be seen as the necessary polarization-dependent perturbation for the development of hydrodynamic instability. In this case, the frequency of the resulting patterns is given by material properties, and, therefore, the amplification and the multipulse feedback is possible following the hydrodynamic scenario.

The interference of the incident light with radiative scattered fields resulting in HSFL-|| are initiated via perpendicularly oriented temperature gradients, which can be induced by non-radiative in-

homogeneous absorption of randomly distributed holes, or laser-induced sub-surface voids [18, 21], or LSFL structures [59]. Their regulation owns to Marangoni convection instability in the form of hydrothermal waves, which drive the hotter melt flow above the initial surface level. The only feasible feedback mechanism of their growth comes from hydrodynamic instability. In contrast, the electromagnetic inter-pulse feedback based on the material removal in the regions with the highest absorbed energy acts destructively on the structures parallel to laser polarization [41, 54]. This is because of the dominant field enhancement at the tips of parallel-oriented periodic nanostructures. HSFL-⊥ are initiated via parallel-oriented temperature gradients, which are dominant in case of large number of bumps or protrusions above the surface. The regulation is driven again by melt flow, however, as soon as formed, the structures can be amplified by ablation feedback, which is favourable for perpendicularly oriented features [41, 54]. The amplification is caused by the dominant field enhancement below the hollows of perpendicular-oriented periodic nanostructures. This way, the non-radiative and radiative fields scattered by holes on metal surface support each other, having the same preferential orientation perpendicular to laser polarization [62]. LSFL-⊥ orientation and periodicity are defined by constructive interference between the incident light and the radiative scattered fields from any type of inhomogeneities, including holes, bumps, or nanoparticles [41, 62]. In this case, the interference is stronger in case of larger nanostructures. The feasible multipulse feedback is ablation, however, melt flow above perpendicularly oriented hot spots of laser absorption below the surface can be as well the driving force for LSFL formation for low fluence and certain materials, such as silicon [63, 104]. Finally, LSFL-⊥ are precursors for grooves-||. Two plausible and contradictory scenarios are relevant here. On one hand, grooves may originate from inhomogeneous energy absorption below the surface [41, 43, 44]. Previously, non-negligible role of radiative field components parallel to laser polarization in case of large surface inhomogeneities on metal surface was evidenced by electromagnetic calculations [62]. The surface waves are retarded by these bumps or holes and result in maxima of the absorbed energy on distances larger than laser wavelength. The coherent superposition of these scattered waves supported by multipulse positive ablation feedback may result in the pat-

Table 1: Types of periodic surface structures on metals and their formation mechanisms

Types of LIPSS	Precursors	Origin of orientation	Origin of periodicity	Feedback
HSFL- \parallel	Laser-induced cavities or LSFL hollows	Hydrothermal waves induced by non-radiative fields	Marangoni convection instability	Melt flow
HSFL- \perp	Pristine bumps or laser-induced protrusions	Hydrothermal waves induced by non-radiative fields	Marangoni convection instability	Melt flow + Possible ablation
LSFL- \perp	Holes, bumps, nanoparticles	Radiative plasmonic or(+) non-plasmonic fields	Interference	Ablation
Grooves- \parallel (electromagnetic)	Irregular LSFL hollows/bumps	Radiative fields	Interference	Ablation
Grooves- \parallel (hydrodynamic)	LSFL hollows	Hydrothermal waves induced by LSFL non-radiative fields	Marangoni convection instability	Melt flow
Hexagonal nanostructures	Hot spots in thin melt layer destabilized by rarefaction	-	Marangoni convection instability	Melt flow + Cavitation
Hexagonal microstructures (spikes)	Hot spots in thick melt layer destabilized by recoil pressure	-	Marangoni convection instability	Melt flow + Ablation

tern establishment with periodicity shifted towards values larger than laser wavelength. This process does not occur concurrently with LSFL formation, therefore, the multipulse ablation of inhomogeneous surface will lead to the genesis of LSFL islands representing supra-wavelength patterns.

On the other hand, LSFL- \perp cause perpendicularly oriented temperature gradients below the surface and generate the hydrothermal waves via surface tension-driven melt flow perpendicularly to these gradients, i. e. parallel to laser polarization [39]. The periods of grooves larger than laser wavelength are the consequence of deeper melt layers below LSFL hollows than in the case when HSFL- \parallel are formed between LSFL structures. Deep melt layers can be achieved for stronger laser fluences but also for higher number of applied pulses, as LSFL structures grow deeper upon multipulse irradiation supported by positive electromagnetic feedback. Finally, hexagonal distribution of nanoholes is attributed to Marangoni instability in destabilized and perturbed thin melt layer. Destabilization occurs mainly due to rarefaction wave and possible cavitation below the surface, where nanoscale perturbations and hot spots are the consequence of non-radiative response of laser-induced nanoholes.

Although we focus on the nanostructures smaller than laser wavelength in this work, the convection instability is likely to be involved in the formation of microstructures, such as periodic grooves, but also quasi-hexagonal arrays of spikes and microholes upon laser irradiation with higher laser energy dose [36, 39, 40, 47–53]. In fact, thicker melt layers $L > 100$ nm with high transverse temperature gradients would be at the origin of the ordering on microscale, with a characteristic period of self-organization $\Lambda \propto 2\pi L$. The time required for the development of such instabilities $\tau_M \approx 10$ ns is realistic under strong ablation conditions, within the measured melt layer lifetime [97]. The application of sequences of double pulses with delays shorter than this characteristic time has already revealed a variety of non-trivial but controllable patterns with dimensions close to laser wavelength [52].

We note also that only temperature-dependent surface tension-driven instabilities are considered in the present work, playing a crucial role at sub-ablation irradiation conditions. In perspective, more advanced models should bring light on the surface dynamics driven by recoil pressure and by material redeposition from plasma plume at stronger ablation conditions and variety of insta-

bilities, which can develop on nanosecond or even larger timescales at micro- and nanoscale, such as Rayleigh-Taylor, Rayleigh-Plateau and Kelvin-Helmholtz instabilities, instability driven by van der Waals forces etc. [18, 20, 33, 36, 37, 50, 105–110].

6. Conclusions

The mechanisms of nanostructure self-organization on metal surfaces upon multipulse femtosecond laser irradiation are investigated by multiphysical approach comprising full-vector Maxwell equations, electron-ion temperature model, and compressible Navier-Stokes equations supported by the equation of state. Simulations performed on initially rough surfaces indicate the non-trivial interaction between light and surface topographies with both electromagnetic and hydrodynamic processes involved in the establishment of subwavelength periodic surface structures. The anisotropic polarization-dependent non-radiative and radiative field distributions around surface inhomogeneities are shown to be at the origin of further surface relief evolution, delivering the orientation dependency towards the final structures. The mechanisms of subwavelength and near-wavelength pattern amplification and regulation, however, appear to be qualitatively different.

Strong local field enhancement, heat confinement, and sub-surface rarefaction result in the development of Marangoni convection instability in a destabilized thin liquid layer. Such an instability is driven by temperature-dependent surface tension forces, triggering material movement and redistribution before the resolidification upon material cooling. In the absence of strong polarization-dependent gradients, quasi-hexagonal convection cells of subwavelength dimensions are assembled, whereas well-oriented temperature gradients contribute to the generation of hydrothermal waves perpendicular to these temperature gradients and formation of high spatial frequency periodic surface structures. The polarization-dependence of the electromagnetic response upon ultrashort laser irradiation is the reason why the instabilities on transverse temperature gradients, taking the form of ripples, dominate over classical cellular convection instability in thin laser-melted layers. The characteristic size of self-organized patterns is defined by Marangoni number and melt layer thickness, but

independent of laser wavelength and surface roughness contrast. The orientation of the resulting patterns is governed by the nature of non-radiative optical response, given by random nanoholes or nanobumps. In case of mixed response, parallel-oriented surface nanostructures dominate, however, the Marangoni convection is also sensitive to thermal properties of metals, affecting the preferable temperature gradient orientation. The growth of the nanostructures is likely to be amplified by rarefaction wave from below or recoil pressure from above.

By introducing the multipulse feedback, we investigate how the redistribution of light on metal surface favors the development of near-wavelength periodic structures, conserving the features of the interference patterns, resulted from coherent superposition of radiative fields on surface roughness. Their regulation is due to ablation feedback mechanism and does not rely on the hydrodynamic instability. We show that the near-wavelength periodic structures can exist concurrently or independently with high spatial frequency patterns, furthermore, can trigger their occurrence or result in their erasure following complex evolution of surface topography and light and matter redistribution.

Commonly observed hierarchical periodic surface structures were obtained and explained by performing multipulse simulations. Among them, HSFL- \parallel grown perpendicular to LSFL crests and HSFL- \perp split from equally oriented LSFL were attributed to the interplay between inhomogeneous absorption on the modified surface and convection instabilities.

The numerical results not only elucidate the mechanisms involved in periodic nanostructure self-organization upon ultrashort laser irradiation, finding the missing link between electromagnetic and hydrodynamic scenarios, but also indicate new possibilities of controlling over Marangoni convection flows, hydrodynamic instabilities, and fabrication of micro- and nanostructures, not limited to ripples but covering a wider class of Turing patterns, via laser-matter excitation and laser-induced melting.

Acknowledgments

This work was supported by IMOTEP project within program 'Investissements d'Avenir' operated by ADEME.

References

- [1] G. M. Whitesides, B. Grzybowski, Self-assembly at all scales, *Science* 295 (5564) (2002) 2418–2421.
- [2] F. T. Arecchi, S. Boccaletti, P. Ramazza, Pattern formation and competition in nonlinear optics, *Physics Reports* 318 (1-2) (1999) 1–83.
- [3] R. S. Bennink, V. Wong, A. M. Marino, D. L. Aronstein, R. W. Boyd, C. R. Stroud Jr., S. Lukishova, D. J. Gauthier, Honeycomb pattern formation by laser-beam filamentation in atomic sodium vapor, *Physical Review Letters* 88 (11) (2002) 113901.
- [4] F. Maucher, T. Pohl, S. Skupin, W. Krolikowski, Self-organization of light in optical media with competing nonlinearities, *Physical Review Letters* 116 (16) (2016) 163902.
- [5] A. Rudenko, J.-P. Colombier, T. E. Itina, From random inhomogeneities to periodic nanostructures induced in bulk silica by ultrashort laser, *Physical Review B* 93 (7) (2016) 075427.
- [6] J.-L. Déziel, L. J. Dubé, S. H. Messaddeq, Y. Messaddeq, C. Varin, Femtosecond self-reconfiguration of laser-induced plasma patterns in dielectrics, *Physical Review B* 97 (20) (2018) 205116.
- [7] A. M. Turing, The chemical basis of morphogenesis, *Phil. Trans. R. Soc. Lond. B* 237 (1952) 37–72.
- [8] Q. Ouyang, H. L. Swinney, Transition from a uniform state to hexagonal and striped Turing patterns, *Nature* 352 (6336) (1991) 610.
- [9] M. C. Cross, P. C. Hohenberg, Pattern formation outside of equilibrium, *Reviews of Modern Physics* 65 (3) (1993) 851.
- [10] I. R. Epstein, B. Xu, Reaction–diffusion processes at the nano- and microscales, *Nature Nanotechnology* 11 (4) (2016) 312.
- [11] J. E. Sipe, J. F. Young, J. S. Preston, H. M. van Driel, Laser-induced periodic surface structure. I. Theory, *Physical Review B* 27 (2) (1983) 1141.
- [12] J. Z. P. Skolski, G. R. B. E. Römer, J. V. Obona, V. Ocelik, A. J. HuisintVeld, J. T. M. De Hosson, Laser-induced periodic surface structures: Fingerprints of light localization, *Physical Review B* 85 (7) (2012) 075320.
- [13] B. Öktem, I. Pavlov, S. Ilday, H. Kalaycıoğlu, A. Rybak, S. Yavaş, M. Erdoğan, F. Ö. Ilday, Nonlinear laser lithography for indefinitely large-area nanostructuring with femtosecond pulses, *Nature Photonics* 7 (11) (2013) 897.
- [14] Z. Liu, J. Siegel, M. Garcia-Lechuga, T. Epicier, Y. Lefkir, S. Reynaud, M. Bugnet, F. Vocanson, J. Solis, G. Vitrant, N. Destouches, Three-dimensional self-organization in nanocomposite layered systems by ultrafast laser pulses, *ACS Nano* 11 (5) (2017) 5031–5040.
- [15] A. Rudenko, C. Mauclair, F. Garrelie, R. Stoian, J.-P. Colombier, Self-organization of surfaces on the nanoscale by topography-mediated selection of quasi-cylindrical and plasmonic waves, *Nanophotonics* 8 (3) (2019) 459–465.
- [16] X. Sedao, M. V. Shugaev, C. Wu, T. Douillard, C. Esnouf, C. Maurice, S. Reynaud, F. Pigeon, F. Garrelie, L. V. Zhigilei, et al., Growth twinning and generation of high-frequency surface nanostructures in ultrafast laser-induced transient melting and resolidification, *ACS Nano* 10 (7) (2016) 6995–7007.
- [17] J. Bonse, S. Höhm, S. V. Kirner, A. Rosenfeld, J. Krüger, Laser-induced periodic surface structures - A scientific evergreen, *IEEE Journal of Selected Topics in Quantum Electronics* 23 (3) (2017) 9000615.
- [18] A. A. Ionin, S. I. Kudryashov, A. E. Ligachev, S. V. Makarov, L. V. Seleznev, D. V. Sinitsyn, Nanoscale cavitation instability of the surface melt along the grooves of one-dimensional nanorelief gratings on an aluminum surface, *JETP Letters* 94 (4) (2011) 266.
- [19] C. S. R. Nathala, A. Ajami, A. A. Ionin, S. I. Kudryashov, S. V. Makarov, T. Ganz, A. Assion, W. Husinsky, Experimental study of fs-laser induced sub-100-nm periodic surface structures on titanium, *Optics Express* 23 (5) (2015) 5915–5929.
- [20] C.-Y. Shih, M. V. Shugaev, C. Wu, L. V. Zhigilei, Generation of subsurface voids, incubation effect, and formation of nanoparticles in short pulse laser interactions with bulk metal targets in liquid: Molecular dynamics study, *The Journal of Physical Chemistry C* 121 (30) (2017) 16549–16567.
- [21] X. Sedao, A. Abou Saleh, A. Rudenko, T. Douillard, C. Esnouf, S. Reynaud, C. Maurice, F. Pigeon, F. Garrelie, J.-P. Colombier, Self-arranged periodic nanovoids by ultrafast laser-induced near-field enhancement, *ACS Photonics* 5 (4) (2018) 1418–1426.
- [22] A. Abou-Saleh, E. T. Karim, C. Maurice, S. Reynaud, F. Pigeon, F. Garrelie, L. V. Zhigilei, J. P. Colombier, Spallation-induced roughness promoting high spatial frequency nanostructure formation on Cr, *Applied Physics A* 124 (4) (2018) 308.
- [23] E. Bodenschatz, W. Pesch, G. Ahlers, Recent developments in Rayleigh–Bénard convection, *Annual review of fluid mechanics* 32 (1) (2000) 709–778.
- [24] J. R. A. Pearson, On convection cells induced by surface tension, *Journal of fluid mechanics* 4 (5) (1958) 489–500.
- [25] M. F. Schatz, S. J. VanHook, W. D. McCormick, J. B. Swift, H. L. Swinney, Onset of surface-tension-driven Bénard convection, *Physical Review Letters* 75 (10) (1995) 1938.
- [26] A. Thess, M. Bestehorn, Planform selection in Bénard-Marangoni convection: 1 hexagons versus 6 hexagons, *Physical Review E* 52 (6) (1995) 6358.
- [27] M. K. Smith, S. H. Davis, Instabilities of dynamic thermocapillary liquid layers. Part 1. Convective instabilities, *Journal of Fluid Mechanics* 132 (1983) 119–144.
- [28] J.-M. Savolainen, M. S. Christensen, P. Balling, Material swelling as the first step in the ablation of metals by ultrashort laser pulses, *Physical Review B* 84 (19) (2011) 193410.
- [29] D. H. Sharp, Overview of Rayleigh-taylor instability, Tech. rep., Los Alamos National Lab., NM (USA) (1983).
- [30] M. Fermigier, L. Limat, J. E. Wesfreid, P. Boudinet, C. Quilliet, Two-dimensional patterns in Rayleigh-Taylor instability of a thin layer, *Journal of Fluid Mechanics* 236 (1992) 349–383.
- [31] C. Li, D. L. Book, Instability generated by acceleration due to rarefaction waves, *Physical Review A* 43 (6) (1991) 3153.
- [32] R. V. Morgan, W. H. Cabot, J. A. Greenough, J. W. Jacobs, Rarefaction-driven Rayleigh–Taylor instability. Part 2. Experiments and simulations in the nonlinear regime, *Journal of Fluid Mechanics* 838 (2018) 320–355.

- [33] S. A. Dyachkov, V. V. Zhakhovsky, A. N. Parshikov, N. A. Inogamov, Ablation into water: Fragmentation of metal via Richtmyer–Meshkov instability, in: *Journal of Physics: Conference Series*, Vol. 1147, IOP Publishing, 2019, p. 012064.
- [34] A. L. Velikovich, Analytic theory of Richtmyer–Meshkov instability for the case of reflected rarefaction wave, *Physics of Fluids* 8 (6) (1996) 1666–1679.
- [35] J. G. Wouchuk, R. Carretero, Linear perturbation growth at the trailing edge of a rarefaction wave, *Physics of Plasmas* 10 (11) (2003) 4237–4252.
- [36] X. Y. Chen, J. Lin, J. M. Liu, Z. G. Liu, Formation and evolution of self-organized hexagonal patterns on silicon surface by laser irradiation in water, *Applied Physics A* 94 (3) (2009) 649–656.
- [37] E. L. Gurevich, Mechanisms of femtosecond LIPSS formation induced by periodic surface temperature modulation, *Applied Surface Science* 374 (2016) 56–60.
- [38] B. J. Kim, K. D. Kim, Rayleigh–Taylor instability of viscous fluids with phase change, *Physical Review E* 93 (4) (2016) 043123.
- [39] G. D. Tsibidis, C. Fotakis, E. Stratakis, From ripples to spikes: A hydrodynamical mechanism to interpret femtosecond laser-induced self-assembled structures, *Physical Review B* 92 (4) (2015) 041405(R).
- [40] G. D. Tsibidis, E. Skoulas, A. Papadopoulos, E. Stratakis, Convection roll-driven generation of supra-wavelength periodic surface structures on dielectrics upon irradiation with femtosecond pulsed lasers, *Physical Review B* 94 (8) (2016) 081305(R).
- [41] J. Z. P. Skolski, G. R. B. E. Römer, J. Vincenc Obona, A. J. Huis in’t Veld, Modeling laser-induced periodic surface structures: Finite-difference time-domain feedback simulations, *Journal of Applied Physics* 115 (10) (2014) 103102.
- [42] S. He, J. J. J. Nivas, K. K. Anoop, A. Vecchione, M. Hu, R. Bruzzese, S. Amoruso, Surface structures induced by ultrashort laser pulses: Formation mechanisms of ripples and grooves, *Applied Surface Science* 353 (2015) 1214–1222.
- [43] H. Zhang, J.-P. Colombier, C. Li, N. Faure, G. Cheng, R. Stoian, Coherence in ultrafast laser-induced periodic surface structures, *Physical Review B* 92 (17) (2015) 174109.
- [44] S. He, J. J. J. Nivas, A. Vecchione, M. Hu, S. Amoruso, On the generation of grooves on crystalline silicon irradiated by femtosecond laser pulses, *Optics Express* 24 (4) (2016) 3238–3247.
- [45] A. Rudenko, J.-P. Colombier, S. Höhm, A. Rosenfeld, J. Krüger, J. Bonse, T. E. Itina, Spontaneous periodic ordering on the surface and in the bulk of dielectrics irradiated by ultrafast laser: a shared electromagnetic origin, *Scientific Reports* 7 (1) (2017) 12306.
- [46] T. T. Dai Huynh, N. Semmar, Dependence of ablation threshold and LIPSS formation on copper thin films by accumulative UV picosecond laser shots, *Applied Physics A* 116 (3) (2014) 1429–1435.
- [47] I. Ursu, I. A. Dorobantu, I. N. Mihailescu, M. Vlad, F. Spineanu, A. M. Prokhorov, V. I. Konov, V. N. Tokarev, Possible mechanism for laser-induced two-dimensional periodic structures by analogy with the Bénard effect, *Optics Letters* 14 (16) (1989) 853–855.
- [48] J. Reif, F. Costache, O. Varlamova, G. Jia, M. Ratzke, Self-organized regular surface patterning by pulsed laser ablation, *Physica Status Solidi C* 6 (3) (2009) 681–686.
- [49] V. I. Emel’yanov, Kuramoto–sivashinsky equation for modulation of surface relief of molten layer and formation of surface periodic microstructures under pulsed laser irradiation of solids, *Laser Physics* 21 (1) (2011) 222–228.
- [50] E. L. Gurevich, Self-organized nanopatterns in thin layers of superheated liquid metals, *Physical Review E* 83 (3) (2011) 031604.
- [51] J.-M. Romano, A. Garcia-Giron, P. Penchev, S. Dimov, Triangular laser-induced submicron textures for functionalising stainless steel surfaces, *Applied Surface Science* 440 (2018) 162–169.
- [52] F. Fraggelakis, G. Mincuzzi, J. Lopez, I. Manek-Hönniger, R. Kling, Controlling 2D laser nano structuring over large area with double femtosecond pulses, *Applied Surface Science* 470 (2019) 677–686.
- [53] J.-G. Son, J. W. Choi, O. Seo, D.-K. Ko, et al., Morphology evolution of self-organized porous structures in silicon surface, *Results in Physics* 12 (2019) 46–51.
- [54] J.-L. Déziel, J. Dumont, D. Gagnon, L. J. Dubé, S. H. Messaddeq, Y. Messaddeq, Constructive feedback for the growth of laser-induced periodic surface structures, *Physica Status Solidi (c)* 13 (2-3) (2016) 121–124.
- [55] Y. Fuentes-Edfuf, J. A. Sánchez-Gil, C. Florian, V. Giannini, J. Solis, J. Siegel, Surface plasmon polaritons on rough metal surfaces: Role in the formation of laser-induced periodic surface structures, *ACS Omega* 4 (4) (2019) 6939–6946.
- [56] M. Garcia-Lechuga, D. Puerto, Y. Fuentes-Edfuf, J. Solis, J. Siegel, Ultrafast moving-spot microscopy: Birth and growth of laser-induced periodic surface structures, *ACS Photonics* 3 (10) (2016) 1961–1967.
- [57] L. Wang, Q.-D. Chen, X.-W. Cao, R. Buividas, X. Wang, S. Juodkazis, H.-B. Sun, Plasmonic nanoprinting: large-area nanoscale energy deposition for efficient surface texturing, *Light: Science & Applications* 6 (12) (2017) e17112.
- [58] J. Reif, O. Varlamova, S. Uhlig, S. Varlamov, M. Bestehorn, On the physics of self-organized nanostructure formation upon femtosecond laser ablation, *Applied Physics A* 117 (1) (2014) 179–184.
- [59] N. A. Kirichenko, E. V. Barmina, G. A. Shafeev, Theoretical and experimental investigation of the formation of high spatial frequency periodic structures on metal surfaces irradiated by ultrashort laser pulses, *Physics of Wave Phenomena* 26 (4) (2018) 264–273.
- [60] A. F. Pan, W. J. Wang, X. S. Mei, H. Z. Yang, X. F. Sun, The formation mechanism and evolution of ps-laser-induced high-spatial-frequency periodic surface structures on titanium, *Applied Physics B* 123 (1) (2017) 21.
- [61] M. Castro, R. Cuerno, L. Vázquez, R. Gago, Self-organized ordering of nanostructures produced by ion-beam sputtering, *Physical Review Letters* 94 (1) (2005) 016102.
- [62] A. Rudenko, C. Mauclair, F. Garrelie, R. Stoian, J. Colombier, Light absorption by surface nanoholes and nanobumps, *Applied Surface Science* 470 (2019) 228 – 233.
- [63] G. D. Tsibidis, M. Barberoglou, P. A. Loukakos, E. Stratakis, C. Fotakis, Dynamics of ripple formation on silicon surfaces by ultrashort laser pulses in sub-ablation conditions, *Physical Review B* 86 (11) (2012) 115316.

- [64] S. Amoruso, G. Ausanio, R. Bruzzese, M. Vitiello, X. Wang, Femtosecond laser pulse irradiation of solid targets as a general route to nanoparticle formation in a vacuum, *Physical Review B* 71 (3) (2005) 033406.
- [65] Y. Shimotsuma, P. G. Kazansky, J. Qiu, K. Hirao, Self-organized nanogratings in glass irradiated by ultrashort light pulses, *Physical Review Letters* 91 (24) (2003) 247405.
- [66] S. Richter, M. Heinrich, S. Döring, A. Tünnermann, S. Nolte, U. Peschel, Nanogratings in fused silica: Formation, control, and applications, *Journal of Laser Applications* 24 (4) (2012) 042008.
- [67] S. M. Petrović, B. Gaković, D. Peruško, E. Stratakis, I. Bogdanović-Radović, M. Čekada, C. Fotakis, B. Jelenković, Femtosecond laser-induced periodic surface structure on the Ti-based nanolayered thin films, *Journal of Applied Physics* 114 (23) (2013) 233108.
- [68] M. H. Dar, R. Kuladeep, V. Saikiran, et al., Femtosecond laser nanostructuring of titanium metal towards fabrication of low-reflective surfaces over broad wavelength range, *Applied Surface Science* 371 (2016) 479–487.
- [69] F. Fraggelakis, G. Mincuzzi, I. Manek-Höninger, J. Lopez, R. Kling, Generation of micro-and nanomorphologies on a stainless steel surface irradiated with 257 nm femtosecond laser pulses, *RSC Advances* 8 (29) (2018) 16082–16087.
- [70] S. Wang, Q. Wu, J. Zheng, B. Zhang, S. Huang, Z. Jia, J. Yao, Q. Zhou, L. Yang, J. Xu, et al., Well-aligned periodic germanium nanoisland arrays with large areas and improved field emission performance induced by femtosecond laser, *Applied Surface Science* (2020) 145308.
- [71] A. Abou Saleh, A. Rudenko, S. Reynaud, F. Pigeon, F. Garrelie, J.-P. Colombier, Sub-100 nm 2d nanopatterning on a large scale by ultrafast laser energy regulation, *Nanoscale* 12 (2020) 6609–6616.
- [72] J.-W. Yao, C.-Y. Zhang, H.-Y. Liu, Q.-F. Dai, L.-J. Wu, S. Lan, A. V. Gopal, V. A. Trofimov, T. M. Lysak, High spatial frequency periodic structures induced on metal surface by femtosecond laser pulses, *Optics Express* 20 (2) (2012) 905–911.
- [73] M. Huang, Y. Cheng, F. Zhao, Z. Xu, The significant role of plasmonic effects in femtosecond laser-induced grating fabrication on the nanoscale, *Annalen der Physik* 525 (1-2) (2013) 74–86.
- [74] J. Song, W. Tao, M. Gong, J. Ye, Y. Dai, G. Ma, J. Qiu, The three-level ripples induced by femtosecond laser on a 6H-SiC single crystal and the formation mechanism, *Applied Physics A* 122 (4) (2016) 450.
- [75] X. Yu, D. Qi, H. Wang, Y. Zhang, L. Wang, Z. Zhang, S. Dai, X. Shen, P. Zhang, Y. Xu, In situ and ex-situ physical scenario of the femtosecond laser-induced periodic surface structures, *Optics Express* 27 (7) (2019) 10087–10097. doi:10.1364/OE.27.010087.
- [76] L. Qi, K. Nishii, Y. Namba, Regular subwavelength surface structures induced by femtosecond laser pulses on stainless steel, *Optics Letters* 34 (12) (2009) 1846–1848.
- [77] K. Liu, X. Li, C. Xie, K. Wang, Q. Zhou, R. Qiu, Formation of sub-200 nm nanostructure on Fe film irradiated by femtosecond laser, *Optics & Laser Technology* 94 (2017) 28–33.
- [78] M. K. Smith, Instability mechanisms in dynamic thermocapillary liquid layers, *The Physics of fluids* 29 (10) (1986) 3182–3186.
- [79] S. Sakabe, M. Hashida, S. Tokita, S. Namba, K. Okamura, Mechanism for self-formation of periodic grating structures on a metal surface by a femtosecond laser pulse, *Physical Review B* 79 (3) (2009) 033409.
- [80] J. Bonse, S. Höhm, A. Rosenfeld, J. Krüger, Sub-100-nm laser-induced periodic surface structures upon irradiation of titanium by Ti: sapphire femtosecond laser pulses in air, *Applied Physics A* 110 (3) (2013) 547–551.
- [81] S. V. Kirner, U. Hermens, A. Mimidis, E. Skoulas, C. Florian, F. Hischen, C. Plamadeala, W. Baumgartner, K. Winands, H. Mescheder, et al., Mimicking bug-like surface structures and their fluid transport produced by ultrashort laser pulse irradiation of steel, *Applied Physics A* 123 (12) (2017) 754.
- [82] A. Talbi, C. T. Tameko, A. Stolz, E. Millon, C. Boulmer-Leborgne, N. Semmar, Nanostructuring of titanium oxide thin film by UV femtosecond laser beam: from one spot to large surfaces, *Applied Surface Science* 418 (2017) 425–429.
- [83] S. I. Anisimov, B. S. Luk'yanchuk, Selected problems of laser ablation theory, *Physics-Uspekhi* 45 (3) (2002) 293.
- [84] A. Rudenko, C. Maclair, F. Garrelie, R. Stoian, J.-P. Colombier, Amplification and regulation of periodic nanostructures in multipulse ultrashort laser-induced surface evolution by electromagnetic-hydrodynamic simulations, *Phys. Rev. B* 99 (2019) 235412. doi:10.1103/PhysRevB.99.235412.
- [85] T. Boeck, A. Thess, Bénard–Marangoni convection at low Prandtl number, *Journal of Fluid Mechanics* 399 (1999) 251–275.
- [86] H. Tomita, K. Abe, Numerical simulation of pattern formation in the Benard–Marangoni convection, *Physics of Fluids* 12 (6) (2000) 1389–1400.
- [87] E. Bévilion, J.-P. Colombier, B. Dutta, R. Stoian, Ab initio nonequilibrium thermodynamic and transport properties of ultrafast laser irradiated 316l stainless steel, *The Journal of Physical Chemistry C* 119 (21) (2015) 11438–11446.
- [88] I. Lomonosov, A. V. Bushman, V. E. Fortov, Equations of state for metals at high energy densities, in: *AIP Conference Proceedings*, Vol. 309, AIP, 1994, pp. 117–120.
- [89] C. S. Kim, Thermophysical properties of stainless steels, Tech. rep., Argonne National Lab., Ill.(USA) (1975).
- [90] R. E. Rozas, A. D. Demirağ, P. G. Toledo, J. Horbach, Thermophysical properties of liquid ni around the melting temperature from molecular dynamics simulation, *The Journal of Chemical Physics* 145 (6) (2016) 064515.
- [91] J. J. Valencia, P. Queded, Thermophysical properties, Modeling for Casting and Solidification Processing 189 (2001).
- [92] C. W. Hirt, B. D. Nichols, Volume of fluid (VOF) method for the dynamics of free boundaries, *Journal of Computational Physics* 39 (1) (1981) 201–225.
- [93] Y. Kawakami, E. Ozawa, S. Sasaki, Coherent array of tungsten ultrafine particles by laser irradiation, *Applied Physics Letters* 74 (26) (1999) 3954–3956.
- [94] Y. Kawakami, E. Ozawa, Self-assembled coherent array of ultra-fine particles on single-crystal tungsten substrate using shg nd: Yag laser, *Applied Physics*

- A 71 (4) (2000) 453–456.
- [95] L. E. Scriven, C. V. Sternling, On cellular convection driven by surface-tension gradients: effects of mean surface tension and surface viscosity, *Journal of Fluid Mechanics* 19 (3) (1964) 321–340.
- [96] L. Y. Barash, T. P. Bigioni, V. M. Vinokur, L. N. Shchur, Evaporation and fluid dynamics of a sessile drop of capillary size, *Physical Review E* 79 (4) (2009) 046301.
- [97] R. Fang, A. Vorobyev, C. Guo, Direct visualization of the complete evolution of femtosecond laser-induced surface structural dynamics of metals, *Light: Science & Applications* 6 (3) (2017) e16256.
- [98] Q. Ouyang, R. Li, G. Li, H. L. Swinney, Dependence of turing pattern wavelength on diffusion rate, *The Journal of chemical physics* 102 (6) (1995) 2551–2555.
- [99] A. K. Horváth, M. Dolnik, A. P. Munuzuri, A. M. Zhabotinsky, I. R. Epstein, Control of turing structures by periodic illumination, *Physical Review Letters* 83 (15) (1999) 2950.
- [100] M. S. Ahsan, M. S. Lee, Formation mechanism of self-organized nanogratings on a titanium surface using femtosecond laser pulses, *Optical Engineering* 51 (12) (2012) 121815.
- [101] J.-P. Colombier, F. Garrelie, N. Faure, S. Reynaud, M. Bounhalli, E. Audouard, R. Stoian, F. Pigeon, Effects of electron-phonon coupling and electron diffusion on ripples growth on ultrafast-laser-irradiated metals, *Journal of Applied Physics* 111 (2) (2012) 024902.
- [102] E. L. Gurevich, Y. Levy, S. V. Gurevich, N. M. Bulgakova, Role of the temperature dynamics in formation of nanopatterns upon single femtosecond laser pulses on gold, *Physical Review B* 95 (5) (2017) 054305.
- [103] Z. Lin, L. V. Zhigilei, V. Celli, Electron-phonon coupling and electron heat capacity of metals under conditions of strong electron-phonon nonequilibrium, *Physical Review B* 77 (7) (2008) 075133.
- [104] M. Schade, O. Varlamova, J. Reif, H. Blumtritt, W. Erfurth, H. S. Leipner, High-resolution investigations of ripple structures formed by femtosecond laser irradiation of silicon, *Analytical and bioanalytical chemistry* 396 (5) (2010) 1905–1911.
- [105] M. H. Emery, J. H. Gardner, J. P. Boris, Rayleigh-Taylor and Kelvin-Helmholtz instabilities in targets accelerated by laser ablation, *Physical Review Letters* 48 (10) (1982) 677.
- [106] A. B. Brailovsky, S. V. Gaponov, V. I. Luchin, Mechanisms of melt droplets and solid-particle ejection from a target surface by pulsed laser action, *Applied Physics A* 61 (1) (1995) 81–86.
- [107] L. K. Ang, Y. Y. Lau, R. M. Gilgenbach, H. L. Spindler, J. S. Lash, S. D. Kovaleski, Surface instability of multipulse laser ablation on a metallic target, *Journal of Applied Physics* 83 (8) (1998) 4466–4471.
- [108] Y. N. Kulchin, O. B. Vitrik, A. A. Kuchmizhak, V. I. Emel'yanov, A. A. Ionin, S. I. Kudryashov, S. V. Makarov, Formation of crownlike and related nanostructures on thin supported gold films irradiated by single diffraction-limited nanosecond laser pulses, *Physical Review E* 90 (2) (2014) 023017.
- [109] S. V. Makarov, V. A. Milichko, I. S. Mukhin, I. I. Shishkin, D. A. Zuev, A. M. Mozharov, A. E. Krasnok, P. A. Belov, Controllable femtosecond laser-induced dewetting for plasmonic applications, *Laser & Photonics Reviews* 10 (1) (2016) 91–99.
- [110] S. Lugomer, Laser-generated Richtmyer–Meshkov and Rayleigh–Taylor instabilities in a semiconfined configuration: bubble dynamics in the central region of the Gaussian spot, *Physica Scripta* 94 (1) (2018) 015001.